

This is a self-archived version of an original article. This version may differ from the original in pagination and typographic details.

Author(s): Pagnanini, L.; Benato, G.; Carniti, P.; Celi, E.; Chiesa, D.; Corbett, J.; Dafinei, I.; Di Domizio, S.; Di Stefano, P.; Ghislandi, S.; Gotti, C.; Helis D., L.; Knobel, R.; Kostensalo, J.; Kotila, J.; Nagorny, S.; Pessina, G.; Pirro, S.; Pozzi, S.; Puiu, A.; Quitadamo, S.; Sisti, M.; Suhonen, J.; Kuznetsov, S.; The ACCESS Collaboration

Title: Array of cryogenic calorimeters to evaluate the spectral shape of forbidden β -decays : the ACCESS project

Year: 2023

Version: Published version

Copyright: © 2023 the Authors

Rights: CC BY 4.0









Rights url: <https://creativecommons.org/licenses/by/4.0/>

Please cite the original version:

Pagnanini, L., Benato, G., Carniti, P., Celi, E., Chiesa, D., Corbett, J., Dafinei, I., Di Domizio, S., Di Stefano, P., Ghislandi, S., Gotti, C., Helis D., L., Knobel, R., Kostensalo, J., Kotila, J., Nagorny, S., Pessina, G., Pirro, S., Pozzi, S., Puiu, A., Quitadamo, S., Sisti, M., Suhonen, J., Kuznetsov, S., The ACCESS Collaboration. (2023). Array of cryogenic calorimeters to evaluate the spectral shape of forbidden β -decays : the ACCESS project. *European Physical Journal Plus*, 138(5), Article 445. <https://doi.org/10.1140/epjp/s13360-023-03946-x>



Array of cryogenic calorimeters to evaluate the spectral shape of forbidden β -decays: the ACCESS project

L. Pagnanini^{1,2,3,a} , G. Benato^{1,2}, P. Carniti^{4,5}, E. Celi^{1,2}, D. Chiesa^{4,5}, J. Corbett³, I. Dafinei¹, S. Di Domizio⁶, P. Di Stefano³ , S. Ghislandi^{1,2,b} , C. Gotti⁵ , D. L. Helis^{1,2}, R. Knobel³, J. Kostensalo⁷ , J. Kotila^{8,9,10} , S. Nagorny³, G. Pessina⁵, S. Pirro², S. Pozzi^{4,5}, A. Puiu², S. Quitadamo^{1,2} , M. Sisti⁵, J. Suhonen⁸ , S. Kuznetsov¹¹,
The ACCESS Collaboration

¹ Gran Sasso Science Institute, 67100 L'Aquila, Italy

² INFN–Laboratori Nazionali del Gran Sasso, 67100 Assergi, L'Aquila, Italy

³ Department of Physics, Engineering Physics and Astronomy, Queen's University, Kingston, ON K7L 3N6, Canada

⁴ Dipartimento di Fisica, Università di Milano-Bicocca, 20126 Milano, Italy

⁵ INFN–Sezione di Milano Bicocca, 20126 Milano, Italy

⁶ Dipartimento di Fisica, INFN Sezione di Genova, Università di Genova, 16146 Genova, Italy

⁷ Natural Resources Institute Finland, Yliopistokatu 6B, 80100 Joensuu, Finland

⁸ Department of Physics, University of Jyväskylä, P.O. Box 35, 40014 Jyväskylä, Finland

⁹ Finnish Institute for Educational Research, University of Jyväskylä, P.O. Box 35, 40014 Jyväskylä, Finland

¹⁰ Sloane Physics Laboratory, Center for Theoretical Physics, Yale University, New Haven, CT 06520-8120, USA

¹¹ Prokhorov General Physics Institute of the Russian Academy of Sciences, 38 Vavilov Str., Moscow, Russia 119991

Received: 21 December 2022 / Accepted: 1 April 2023

© The Author(s) 2023

Abstract The ACCESS (Array of Cryogenic Calorimeters to Evaluate Spectral Shapes) project aims to establish a novel technique to perform precision measurements of forbidden β -decays, which can serve as an important benchmark for nuclear physics calculations and represent a significant background in astroparticle physics experiments. ACCESS will operate a pilot array of cryogenic calorimeters based on natural and doped crystals containing β -emitting radionuclides. In this way, natural (e.g. ^{113}Cd and ^{115}In) and synthetic isotopes (e.g. ^{99}Tc) will be simultaneously measured with a common experimental technique. The array will also include further crystals optimised to disentangle the different background sources, thus reducing the systematic uncertainty. In this paper, we give an overview of the ACCESS research program, discussing a detector design study and promising results of ^{115}In .

1 Introduction

Since its debut in the scientific community, the neutrino has played a crucial role in the puzzle of fundamental particles, due to its peculiar cocktail of properties: at the same time the neutrino is the lightest massive particle of the Standard Model, the most elusive one, and the only neutral fundamental fermion. Particularly, this last feature makes the neutrino the perfect probe for Majorana's hypothesis, according to which a fermion and its own antiparticle have the same real wave function. Indeed, we can distinguish a neutrino from an antineutrino only indirectly, through its interactions in matter. They could be two different states of the same particle, which interacts in two different ways according to its chirality. The discovery of neutrino oscillations, revealing its massive nature, has pushed the experimental efforts in this direction, because only a massive particle can reverse its chirality.

As far as we know, the only process that could unravel the mysterious nature of neutrino is the neutrinoless double beta decay ($0\nu\beta\beta$). It is a forbidden, lepton-number-violating nuclear transition, whose observation would answer long-standing questions, such as Dirac or Majorana nature of neutrinos and their absolute mass, also providing a possible leptogenesis mechanism to explain matter–antimatter asymmetry in the Universe. The $0\nu\beta\beta$ would be an extremely rare decay, making its searches exceptionally challenging. In the case of light Majorana mass exchange mechanism, according to Fermi's golden rule, its half-life can be factorised as:

$$\left(T_{1/2}^{0\nu}\right)^{-1} = g_A^4 G^{0\nu}(Q_{\beta\beta}, Z) \left| \mathcal{M}^{0\nu}(A, Z) \right|^2 \left| \frac{m_{\beta\beta}}{m_e} \right|^2 \quad (1)$$

Focus Point on Advances in Cryogenic Detectors for Dark Matter, Neutrino Physics and Astrophysics Guest editor: L. Pattavina.

^a e-mail: lorenzo.pagnanini@gssi.it (corresponding author)

^b e-mail: stefano.ghislandi@gssi.it (corresponding author)

where $\mathcal{G}^{0\nu}(Q_{\beta\beta}, Z)$ is the phase-space factor, g_A is the axial-vector coupling strength, $\mathcal{M}^{0\nu}(A, Z)$ is the nuclear matrix element (NME), m_e is the electron mass, and $m_{\beta\beta}$ is the effective Majorana mass of the neutrino. The latter is the New Physics parameter that we can derive from Eq. (1), provided that we know all the involved variables. The phase-space factor depends on the decay kinematics, and its value is calculated with a high precision for each isotope [1, 2]. On the contrary, the uncertainties of the theoretical estimates for the NME are large, at least of the order of 30% based on the variation between the NME values provided by various theoretical frameworks adopting different approaches to solve the nuclear many-body problem [3–5].

Further evidence that nuclear theory has room for improvement is the fact that a *quenching* of the free-nucleon axial coupling constant, $g_A^{\text{free}} = 1.27641$ [6], is usually required to bring theory in agreement with β -decay experimental data within some theoretical models. The same holds for two-neutrino double beta decay ($2\nu\beta\beta$) [5], the standard-model allowed counterpart of the $0\nu\beta\beta$. Whether the quenching found for β -decay and $2\nu\beta\beta$ applies similarly to the $0\nu\beta\beta$ is still a matter of debate [7, 8]; indeed, these nuclear processes have a low-momentum exchange, while $0\nu\beta\beta$ is a high-momentum exchange process involving states up to ~ 100 MeV. Though it is not obvious how the quenching in $2\nu\beta\beta$ generalises to $0\nu\beta\beta$, it is of utmost importance to study the quenching of g_A with different approaches to identify its origin and to understand the implications of it when probing new physics phenomena.

In this scenario, new experimental data to benchmark nuclear model calculations are pivotal. Indeed, if a next-generation experiment observes the $0\nu\beta\beta$ decay, the NME uncertainty will directly reflect on the Majorana mass, and on the half-lives predicted for other isotopes. On the other hand, if next-generation experiments fail to observe $0\nu\beta\beta$ decay, the scientific community would know which are the most favoured isotopes to steer the subsequent efforts, but again NME uncertainties complicate the selection process. For this reason, the Astro Particle Physics European Committee (APPEC) in its recent report on European Strategy for $0\nu\beta\beta$ recommends “A dedicated theoretical and experimental effort, in collaboration with the nuclear physics community to achieve a more accurate determination of the NMEs” [9]. This is exactly what the ACCESS project aims to do.

There are several ways to quantify the effective quenching in decay processes with low-momentum exchange, such as discussed in Refs. [7, 10]. One of the proposed methods exploits the dependence of the β -spectrum shape of forbidden non-unique beta transitions on the g_A value. Since in these particular decays high multipolarities are involved, as in $0\nu\beta\beta$, they are an attractive tool to investigate the nuclear aspects of this transition. A detailed review of theoretical and experimental achievements in this field can be found in Ref. [8]. Moreover, several experimental searches in astroparticle physics are affected by assumptions regarding the β -decay spectral shape, such as the ^{210}Bi in solar neutrino detection [11], ^{39}Ar in dark-matter search with liquid argon-based detectors [12], and ^{90}Sr in cryogenic calorimeters [13–15]. A precise evaluation of the spectral shape of these background components would notably reduce the systematic uncertainty in the data modelling and improve the experimental sensitivity.

In this field, the main experimental efforts focused on naturally occurring isotopes for which a forbidden non-unique β -decay is expected: ^{113}Cd , ^{115}In , and ^{50}V . ^{113}Cd β -decay is the most studied process, thanks to well-established experimental methods. The most accurate measurement was performed by the KINR-DAMA collaboration at the Laboratori Nazionali del Gran Sasso (LNGS) by using a CdWO_4 scintillating crystal in long-term low-background measurements. The shape of the spectrum was precisely measured with an energy threshold of 28 keV, an energy resolution of 47 keV at $Q_\beta = (323.83 \pm 0.27)$ keV [16], and a signal-to-background ratio of ~ 56 [17]. Recently, the COBRA collaboration carried out a very precise measurement with CdZnTe (CZT) semiconductor detectors, achieving an energy threshold of 84 keV, an energy resolution of 18 keV at Q_β , and a signal-to-background ratio of ~ 47 [18]. ^{50}V presents an opposite situation, having its β -decay not yet observed. Different experimental approaches are under development [19, 20] to investigate such decay beyond the current limit, i.e. $T_{1/2} > 1.9 \times 10^{19}$ yr [19]. For ^{115}In , there were two measurements based on scintillating liquid loaded with In [21, 22], and LiInSe_2 cryogenic calorimeter [23]. While the former measurement featured a poor energy resolution and energy threshold which prevented a detailed study of the spectral shape, this was successfully performed in the latter case. This is a further confirmation that cryogenic macro-calorimeters are a proper tool to assess the spectral shape of β -decay, as extensively demonstrated in last years for the two-neutrino double beta decay [13–15, 24]. The success of these efforts led to the idea of applying cryogenic calorimeters to spectral shape measurements of rare β -decays. There are other alternative or complementary experimental approaches based on Metallic Magnetic Calorimeters [25] or Silicon Drift Detectors [26, 27] which are consolidating, reflecting the growing interest in this research field.

In this work, we introduce the ACCESS project, providing a general overview of the research program. In Sect. 2 we introduce the spectral shape method, and in Sects. 3 and 4 we detail the features of crystals and sensors, respectively. In Sect. 5 we describe the Monte Carlo techniques adopted for the ACCESS purpose, in particular for the performance study presented in Sect. 6. Finally, we discuss the preliminary results of the ACCESS measurements in Sect. 7, and the project perspectives in Sect. 8.

2 Theoretical framework

The Spectral Shape Method (SSM) [28] is based on the fact that for forbidden non-unique β -decays the energy spectrum of the emitted electrons—described by the β -decay shape function—depends on the leptonic phase-space factors and the Nuclear Matrix Elements (NMEs) in a non-trivial way. The phase-space factors can be calculated to a desired accuracy [29], but the NMEs are subject to systematic uncertainties of the underlying nuclear models.

The complexities of the shape function are condensed in the so-called shape factor $C(w_e)$, which is a function of the total energy w_e of the emitted electron (in units of the electron rest mass) [10, 28]. The shape factor can be divided into an axial-vector part $C_A(w_e)$, a vector part $C_V(w_e)$, and a mixed vector-axial-vector part $C_{VA}(w_e)$, such that we obtain

$$C(w_e) = g_A^2 \left[C_A(w_e) + \left(\frac{g_V}{g_A} \right)^2 C_V(w_e) + \frac{g_V}{g_A} C_{VA}(w_e) \right]. \quad (2)$$

Here the interference between the sum of the C_A and C_V parts and the mixed C_{VA} part causes a variation of the electron spectral shapes depending on the ratio g_V/g_A .

In [28] it was noticed that the variation was rather strong for the β -decay transition $^{113}\text{Cd}(1/2^+) \rightarrow ^{113}\text{In}(9/2^+)$ when the NMEs were computed by using the interacting shell model (ISM) [30] and the microscopic quasi-particle-phonon model (MQPM) [31]. In a further study of this transition [32], a similar dependence was recorded for the microscopic interacting boson-fermion model (IBFM-2) [33]. The essence of the SSM philosophy is to compare the electron spectral shapes, computed for different values of g_A , with the measured one in order to be able to access an effective value of g_A . In Ref. [32] the computed electron spectra are compared with the one measured in Ref. [17], finding that the measured spectrum is roughly reproduced by the calculated spectra of all three nuclear models for values of $g_A/g_V \sim 0.9$. This is a remarkable result if we consider the totally different nuclear-structure principles behind these models.

In the studies [28, 32], as also in Ref. [18], it was noticed that a simultaneous prediction of the electron spectral shape and the partial half-life of the decay transition was a challenge. In Ref. [34], it was proposed to use the conserved-vector-current hypothesis (CVC)-related NME, introducing the so-called small relativistic NME [35] (here denoted as “s-NME”), to fix the problem with the prediction of the partial half-life of the decay transition simultaneously with the β -decay spectral shape. This “enhanced SSM” was successfully tested in the work [36] for the ^{113}Cd decay using the three mentioned nuclear models, and further applications were presented in [37]. To the recently measured ^{115}In decay [23] the enhanced SSM was not yet applied, but in the ACCESS project we are going to harness the full power of this method in order to obtain fine-tuned results for ^{115}In and other potentially interesting nuclei.

The value of the s-NME is directly related to the CVC in an ideal calculation [35]. The magnitude of the CVC-based s-NME is typically 2–3 orders of magnitude smaller than the magnitude of a typical main NME which collects strong contributions from the $1\hbar\omega$ shell-model valence space [37]. Instead, the s-NME collects its contributions from beyond the $1\hbar\omega$ valence space, making the prediction of its value very hard for the nuclear models used in the SSM calculations. In particular, due to their very restricted valence spaces, the ISM and IBFM-2 typically predict a zero value for the s-NME [37]. The MQPM, instead, has a large valence space but still it predicts too small magnitudes for the s-NME. Despite its small value, the s-NME plays a role in determining the half-life of a beta transition. This is why it is important to have an estimate of its value, and its CVC value is a good reference in the enhanced SSM calculations.

Since the CVC value of the s-NME requires an “absolute” calculation (infinite valence space, perfect many-body theory, etc.) it cannot be used directly in realistic applications. Instead, it can be used as a free parameter and its value can be adjusted to reproduce the experimental partial half-life of the beta transition of interest. This adjustment has to be done for each value of g_A separately so that the computed beta-spectrum templates used in the enhanced SSM will fix both g_A and s-NME when matched with the experimental beta spectrum. The thus fixed value of the s-NME is typically in the ballpark of its CVC value [37].

3 Crystals

The ACCESS project proposes to use different crystals to measure the spectral shape of different β -emitters. A list of isotopes interesting for Nuclear and Astroparticle Physics is presented in Table 1.

Natural crystals Only three forbidden β -decay emitters are natural isotopes with a high isotopic abundance (i.a.); ^{115}In (i.a. = 95.72%), ^{113}Cd (i.a. = 12.23%), and ^{87}Rb (i.a. = 27.835%). In particular, the first two isotopes can be embedded in crystals suitable to be used as an absorber in a cryogenic calorimeter, such as indium oxide (In_2O_3) [38], indium iodide (InI), and cadmium tungstate (CdWO_4). These are the first crystals and isotopes to which ACCESS will focus on. Another interesting candidate to explore as cryogenic calorimeter for the ACCESS purposes could be the PbWO_4 , the material used for the electromagnetic calorimeter of the Compact Muon Solenoid (CMS) [39] experiment at Large Hadron Collider (LHC). The residual amount of ^{210}Pb from natural radioactivity in such crystal could allow one to study the low-energy β -decay of ^{210}Pb , and the subsequent decay of ^{210}Bi . This material is currently under investigation for RES NOVA, a proposed experiment to detect Supernova Neutrinos with PbWO_4 based cryogenic calorimeters at LNGS [40, 41].

Doped crystals Unfortunately, natural crystals would allow to study only a limited number of isotopes belonging to the long list of interesting candidates. A different approach is therefore needed to develop a technique able to assess simultaneously a higher number of isotopes. Based on previous successful experience with doped crystal to study α -decay [42], we propose to have a *carrier crystal*, e.g. TeO_2 or Li_2MoO_4 , doped with a specific β -decaying isotope during the crystal growth. For each isotope, a twin pair of crystals, one doped and one natural can be operated simultaneously. While the embedded β -source will dominate the counting rate of the doped crystal, the natural one will monitor internal and environmental backgrounds. A combined fit of Monte Carlo

Table 1 List of the isotopes whose β -decay could be measured using the carrier crystal approach proposed by ACCESS (in bold) or natural crystals

Physics case	Isotope	Q_β (keV)	Half-life (year)	Natural abundance or target doping
Nuclear physics	⁹⁹ Tc	293.8	2.11×10^5	0.25 ppb
	¹¹³ Cd	316	7.70×10^{15}	13.47%
	¹¹⁵ In	496	4.41×10^{14}	95.7%
	⁹⁰ Sr	545.9	28.8	30 ppq
Background in ν -physics and dark matter search	³⁹ Ar	565	269	0.15 ppt
	⁴² Ar	599	32.9	20 ppq
	²¹⁰ Bi	1161.2	0.014	²³⁸ U decay chain
Cosmic neutrino background detection	¹⁵¹ Sm	76.4	94.7	0.20 ppt
	²¹⁰ Pb	63.5	22.2	²³⁸ U decay chain

In the rightmost column, we report the isotopic abundance of naturally occurring isotopes, and the target activity of artificial isotopes in doped crystals. ²¹⁰Pb and ²¹⁰Bi belong to ²³⁸U natural radioactive chain, so that their spectra can be measured with natural PbWO₄ exploiting the residual ²¹⁰Pb contamination

simulations to the two spectra will ensure a precise reconstruction of both signal and background spectral shapes. For each isotope, the crystal size will be determined by balancing the containment efficiency of the β -signal, and the background rate in the region of interest. Given the Q -value of the considered processes (< 600 keV), a 1 cm³ TeO₂ crystal would be a reasonable candidate as a carrier crystal. Therefore, we use this as a reference for our β -source concentration calculations. Indeed, the powder doping can be tuned in order to optimise the signal rate (e.g. ~ 2 Hz) without spoiling the bolometric performance. As reported in Table 1, the target doping to get a signal rate of ~ 2 Hz in a 1 cm³ TeO₂ crystal is at most at ppb level, giving a negligible contribution to the detector heat capacity. The main challenge of this approach is to obtain uniform doping in the crystal volume to ensure a correct evaluation of the detection efficiency. For this reason, several doping tests will be needed to study source segregation, and eventually, the optimal configuration will be reached after several growths. The goal of ACCESS is to demonstrate the potential of this technique at least with an isotope, reasonably ⁹⁹Tc.

4 Thermal sensors

The natural choice for the ACCESS thermal sensors is semiconductor thermistors, i.e. Neutron Transmutation-Doped germanium (Ge-NTD or NTD) [43], developed and successfully operated by CUORE, CUPID-0 and CUPID-Mo collaborations. Ge-NTDs are obtained by doping an ultra-pure germanium slab up to a concentration close to the critical value for the metal-insulator transition [44]. In this condition, below $\simeq 1$ K, the electrical conductivity is driven by the Variable-Range Hopping (VRH) mechanism [45], and the relation between electrical resistivity (ρ) and temperature (T) is described by the Mott law [46]:

$$\rho(T) = \rho_0 \exp\left(\frac{T_0}{T}\right)^{\frac{1}{2}} \quad (3)$$

ρ_0 is a parameter that depends on the intrinsic properties of the germanium lattice, while T_0 depends on the uniformity and concentration of the doping. Through the variation of its resistance (Fig. 1 left), the NTD converts a temperature variation, induced by an energy deposition in the crystal, into an electric signal.

The NTD is operated by biasing it with a potential difference V_{bias} through an electric circuit where each sensor is connected in series with a load resistor $R_{\text{load}} \gg R$, as reported in Fig. 1 (left). In this way, for any bias voltage V_{bias} , the current flowing through the thermistor can be assumed to be constant. The optimal working point is chosen maximising the SNR by scanning a voltage region where the NTD response is still linear.

In underground astroparticle physics, NTD-based cryogenic calorimeters are usually operated at temperatures of the order of 10 mK to reduce the heat capacity of the absorber, thus enhancing the signal amplitude. NTDs feature a high dynamic range, allowing them to detect energy depositions over a wide interval, from few keV up to $\simeq 10$ MeV, and a very good energy resolution, of the order $\simeq 0.2$ – 0.3% [48, 49]. However, they are characterized by a relatively slow time response, so thermal pulses develop over a time interval that ranges from hundreds of ms up to few seconds (depending also on the heat capacity of the crystals) [48]. Therefore, a bolometer read out by NTDs can be affected by pile-up between different thermal pulses. Since the energy of two piled-up signals cannot be precisely reconstructed, these events are rejected reducing the selection efficiency in high-rate measurements (> 1 Hz) [23].

In natural crystals, the signal counting rate is determined by the crystal dimensions, which can be optimised to increase the signal-to-background ratio. Since the expected counting rate due to β -signal and radioactive backgrounds in this application is $\mathcal{O}(200$ mHz), NTD readout is very suitable. Indeed, with a time resolution at a level of few ms and a time acquisition window of 500 ms [38], the pileup probability is below 10%.

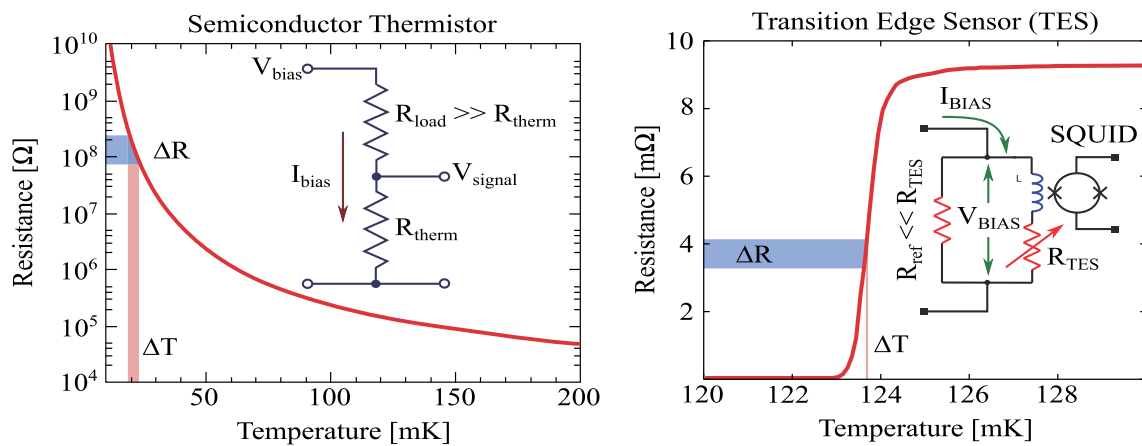


Fig. 1 Resistance as a function of the NTD (left) and TES (right) temperature. A simplified scheme of the bias circuit for the two sensors is also shown. R_{therm} and R_{TES} represent the resistance of the NTD and the TES, respectively. Figure adapted from [47]

Table 2 Detector performance used in the Monte Carlo simulation processing for NTD [59] and TES sensors [55, 56]

Parameter	NTD	TES
Rise time	10 ms	1 ms
Acquisition window	1 s	100 ms
Energy resolution	1 keV	100 eV
Energy threshold	5 eV	1 eV

These parameters can vary from one detector to another depending on the features of sensor, absorber, and their coupling. For this reason, we chose as reference performance that of detectors as similar as possible to those foreseen for ACCESS

Doped crystals exhibit a signal counting rate dependent on the source concentration, which can be adjusted by balancing the high signal-to-background ratio and the low pileup probability. In this case, NTD sensor may not be the most effective choice, because the slow time response limits the maximum tolerable activity to $\mathcal{O}(1 \text{ Hz})$. The Transition Edge Sensors (TES) can overcome such limitations.

A TES is a thin film made of a superconducting material, operated at a temperature just below its superconducting transition temperature so that its resistivity is negligible. When an energy deposition occurs in the absorber to which the TES is coupled, the induced rise in temperature causes the resistance of the TES to increase, following the superconductive-to-normal metal transition (see Fig. 1 right). Since the transition lies in a temperature range of $\sim 1 \text{ mK}$, the TES is extremely sensitive also to very small energy depositions, featuring excellent energy resolution and extremely low energy threshold. The values of these parameters depend a lot on the different sensor optimisations performed for the specific physics case [50–56]. Another advantage of TES is that they are sensitive to athermal phonons rather than thermal phonons (like is the case for NTDs), therefore, their time response is faster than the one of the NTD, but also, in this case, the actual value depends on the specific application. For the purposes of this paper, we assume the TES performance obtained in Refs. [55, 56] and reported in Table 2, because they have been achieved with detectors similar to the ACCESS ones. For ACCESS purposes, it would be very useful to combine the two temperature sensors operating them together and in two different dynamic ranges. The NTD readout provides data useful for the internal background reconstruction via α -spectroscopy while data collected with TES readout allows mitigating the pileup in the signal. Operating NTD and TES on the same crystal featuring a high counting rate would also enable the possibility to study and improve the pileup rejection efficiency achieved with NTD, which is of pivotal importance for the CUPID $0\nu\beta\beta$ next-generation experiment [57, 58].

5 Monte Carlo simulations

Given a certain β -decaying isotope to be measured, the corresponding detector design can be optimised by means of Monte Carlo simulations. Hereafter, we describe the software tools we plan to use for this purpose, while their application to the sample case study of ^{115}In is reported in Sect. 6.

We simulate the signal and the different background sources with a Monte Carlo toolkit, called *Arby*, based on the GEANT4 framework [60], version 4.10.03. The radioactive decay from the various sources can be generated in any volume or surface of the detector, cryostat and shielding implemented in *Arby* [61]. The primary and any secondary particles are then propagated through the detector geometry using the Livermore physics list. The energy deposited in crystals is recorded in the Monte Carlo output together

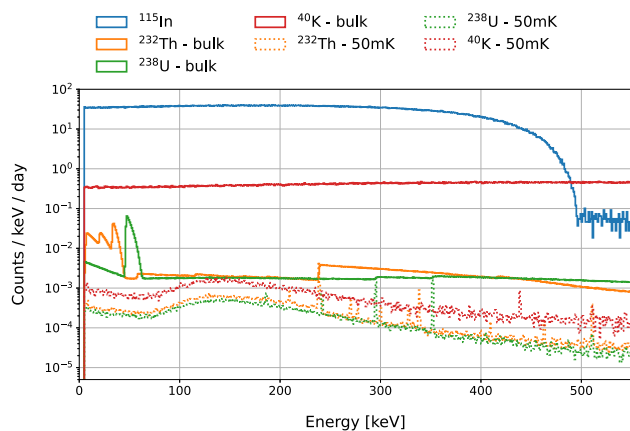


Fig. 2 Simulated energy spectra of the ¹¹⁵In β-decay (blue), and the different background components for a 7 mm-side InI crystal with NTD readout. We include in this plot only the dominant background contributions, i.e. the bulk contaminations of the crystal and the thermal shield at 50 mK. As expected, the ¹¹⁵In β-decay is two orders of magnitude higher with respect to the limit on the ⁴⁰K background (solid red)

with the time at which the interaction occurred. The fraction of energy released by any particle type is also recorded to allow particle identification. Radioactive decays are implemented using the G4RadioactiveDecay database. The decay chains of ²³²Th, ²³⁸U, and ²³⁵U can be simulated completely or in part, to reproduce breaks of secular equilibrium. The β-decay simulations are generated according to the energy spectral shape templates, obtained as described in Sect. 2.

In order to implement the detector response function and data production features in the Monte Carlo data, we reprocess the *Arby* output with a dedicated code. In particular, to account for detector time resolution, we sum energy depositions that occur in the same crystal within the signal rise time. We reproduce the single signal selection defining a pile-up window¹ around each event: if another signal falls in it we discard both the events as in the data processing. The experimental energy resolution is usually reproduced by applying a Gaussian smearing function with linearly variable width based on measured FWHM of γ-ray and α-particle peaks, while the energy threshold of each detector is modelled with an error function that interpolates the experimental data of trigger efficiency versus energy. In the specific case of the study presented in Sect. 6, we assume a constant energy resolution (σ) and a conservative energy threshold of 5σ. The selection and detection efficiencies are calculated on the data as a function of the energy, and modelled with an error function which is applied to the Monte Carlo simulations.

6 Detector design studies: the In-115 case

With the Monte Carlo tools just described, we conduct a study to optimise the detector design of an indium iodide crystal. We evaluate the side size of the crystal by optimising the interplay between signal and background rates. The signal simulation takes as input a theoretical energy spectrum template with fixed s-NME = 2.0 and g_A = 0.9, which are assumed to be reasonable values according to a previous enhanced-SSM analysis on ¹¹³Cd [36]. For this study, we consider in our simulations InI cubic crystals of different sides in the range 2–10 mm, computing the expected activity accordingly:

$$A(\text{Bq}) = \frac{N_0}{\tau} = \frac{d \cdot l^3 \cdot N_A \cdot i.a.}{M \cdot \tau} \tag{4}$$

where *d* is the InI density, *l* the crystal side, *N_A* is the Avogadro number, *M* the InI molar mass, while *i.a.* and τ are the isotopic abundance and the mean-life of ¹¹⁵In, respectively.

On the background side, we expect ²³²Th, ²³⁸U chains and ⁴⁰K to be the most prominent contributions. Therefore, we simulate these radioactive sources in the thermal shields of the cryostat, characterised by the CUORE-0 and CUPID-0 experiments [61], and in the crystal bulk. For the latter, we compute quite conservative limits exploiting the InI data shown in Sect. 7. Typical performance of detectors similar to the ones we expect to use are reported in Table 2.

The resulting energy spectra for an InI crystal of size 7 × 7 × 7 mm³, shown in Fig. 2, demonstrates that the expected background level is low enough to ensure a clear assessment of the β-decay spectral shape. In order to understand which are the optimal crystal dimensions, for each configuration, we integrate the energy spectrum of signal and background in the energy interval from 0 keV up to the Q-value of the ¹¹⁵In β-decay. The resulting signal and background throughput, together with the signal-to-background ratio, are reported in Fig. 3.

¹ The pile-up window reproduces the experimental data time acquisition window, which is not always symmetrical with respect to the trigger position (see Fig. 8 left).

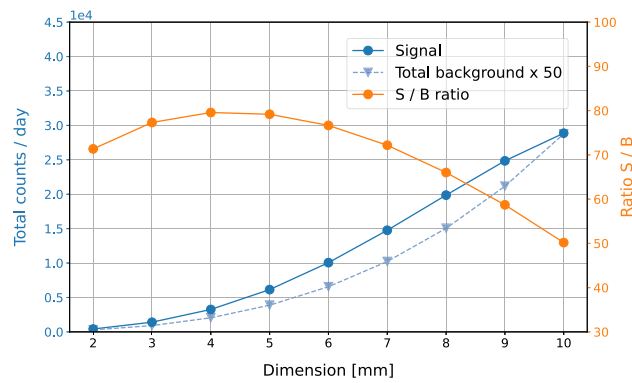


Fig. 3 Signal rate (blue solid line), limit on background rate (blue-dashed line), and signal-to-background ratio (orange solid line) as a function of the absorber side. The signal rate grows with the dimension even if, for larger sizes, the occurrence of multiple decay within the same acquisition time window reduces the efficiency of signal selection. The limit on the background increases almost linearly with the crystal volume, thus the signal-to-background ratio is more favourable for small crystals

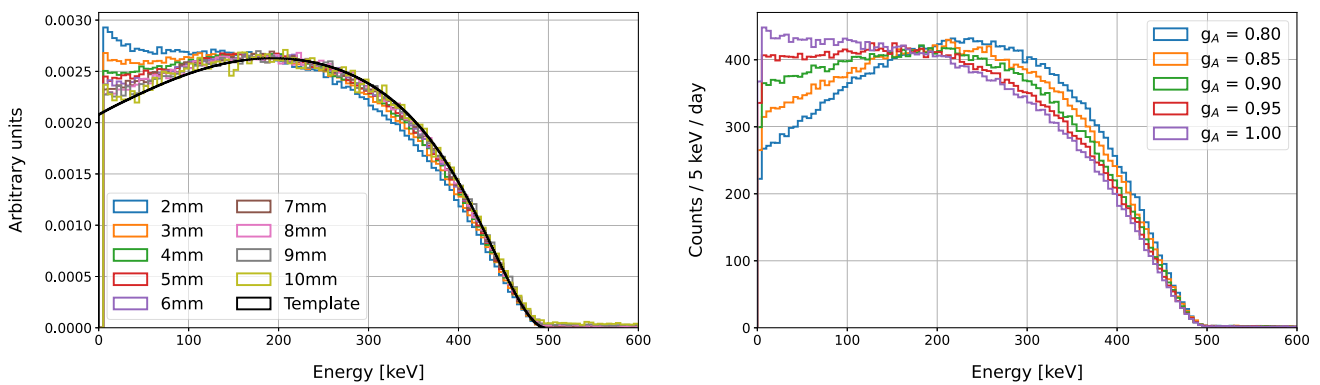


Fig. 4 Simulated energy spectra of the ^{115}In β -decay for different dimensions of the absorber (assuming $s\text{-NME} = 2.0$ and $g_A = 0.9$, left). The larger is the crystal the lower is the difference between the template spectrum (black) and the simulated one. The simulation for the 7 mm side crystal is repeated for five different values of g_A around the chosen reference value (right). The simulations are processed introducing the detector performance reported in Table 2

The signal rate increases with the size of the crystal due to a larger indium activity, allowing the collection of more statistics. However, the effect of the pile-up is not negligible for larger absorbers, thus damping the previous trend. This happens when the mean time between subsequent events becomes comparable with the acquisition window length of 1 s. The background rate, instead, being dominated by bulk contamination, always gets larger with the crystal dimensions. As a result, the signal-to-background ratio reaches its maximum at absorber size, of ~ 4 mm and then decreases, as shown in Fig. 3. Thus, little absorbers are preferred from the signal-to-background point of view. However, larger absorbers, beside the higher absolute signal rate, are characterised by a higher containment efficiency, useful in the fit procedure to better identify and fix background peaks. Taking everything into account, we consider a crystal of 7 mm side size a good compromise to maximise the signal rate and the background modelling efficacy while keeping a satisfying signal-to-background ratio.

Another crucial point of this study is the evaluation of the detector response function on the β -decay spectrum, because we want to avoid any distortions introduced for example by the pile-up. This is important to understand if the thermal sensors we are taking into account, NTD and TES, are suitable for our purposes. First of all, we want to minimise the partial containment of the signal, to be sure that the detector response function does not deteriorate our sensitivity to different g_A . In Fig. 4, we show ^{115}In spectra generated for different sizes of the absorber (left), and different axial coupling constants (right). In order to be conservative, we look at them by considering in the Monte Carlo simulations the typical parameters of the sensor with poorer performance, i.e. the NTD reported in Table 2. Even if the detector response function can be effectively evaluated by Monte Carlo simulations, as demonstrated in several works [61], we can conclude that larger crystals are preferred in order to minimise the effects due to partial containment, thus reducing any possible systematic uncertainty due to the detector response function.

Two other essential parameters to be considered are the energy resolution and the energy threshold. Typically the better the energy resolution is, the lower the detector energy threshold will be. Let us fix the theory input as before: $s\text{-NME} = 2.0$ and $g_A = 0.90$, the time resolution (10 ms) and the acquisition window (1 s). We take into account 4 different constant energy resolutions: 200 eV, 1 keV, 5 keV and 10 keV. As a rule of thumb, we assign an energy threshold equal to 5 times the energy resolution, so respectively 1 keV, 5 keV, 25 keV and 50 keV. The simulated spectra processed with these parameters are presented in Fig. 5. A worsening in the energy resolution is not affecting the spectral shape, our signal being a continuum spectrum. Nevertheless, a better energy resolution

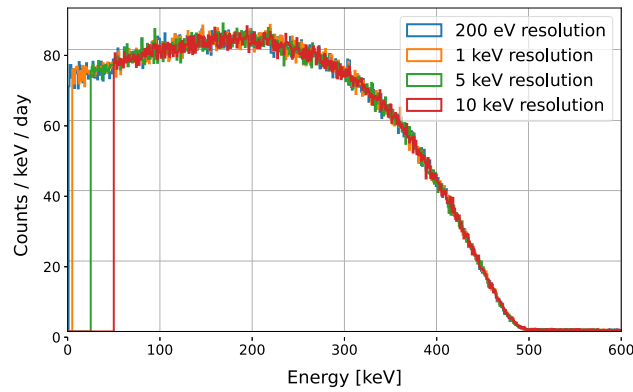


Fig. 5 Effect of different energy resolution and energy thresholds on the ^{115}In spectrum. Notice that the first parameter has no repercussions on the resulting shape

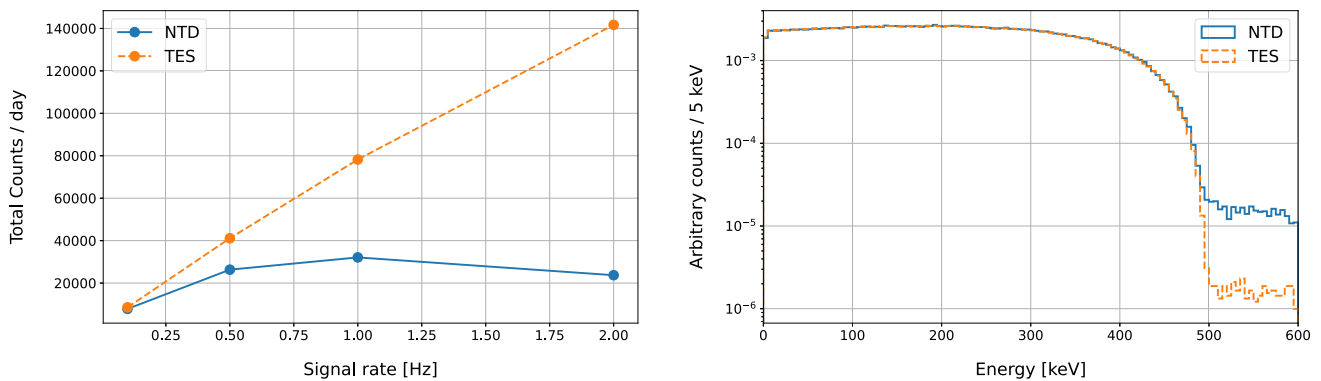


Fig. 6 *Left.* Expected signal counts per day as a function of the source activity assuming time and energy resolutions of a NTD (blue solid line) and a TES (orange-dashed line). The divergence from the linear trend grows with the expected signal rate due the presence of multiple signals in the same acquisition time window. *Right.* Energy spectra of the ^{115}In β -decay assuming time and energy resolutions of a NTD (blue solid line) and a TES (orange-dashed line). As expected, the piled up events populate the energy spectrum above the ^{115}In Q -value in the NTD case, while the pileup is practically negligible for the TES

helps to fix the different background sources in the spectrum reconstruction. Conversely, an energy threshold larger than 50 keV cuts away a good fraction of the low energy region, where the spectral shape effects due to a different value of g_A are more relevant. Thus, both the thermal sensors considered in this paper are suitable for these studies as long as the energy threshold is lower than 50 keV.

Lastly, we study the effects of different timing parameters, i.e. the time resolution and the acquisition window length. A good time resolution allows us to distinguish pulses close in time that would be integrated together otherwise. Moreover, faster pulses ensure shorter acquisition intervals, reducing the statistical loss due to multiple pulses in the same window, usually discarded during the data analysis. TES operated with macro-calorimeters of the size mentioned above, usually have rise times in the order of 1 ms. We decide cautiously to consider a time resolution equal to the rise time itself since the resolution heavily depends on the algorithm used to tag overlapped pulses, even if it can be reduced up to 10 times with sophisticated analyses [62]. With a signal rate of $\gtrsim 1$ Hz, the presence of multiple pulses within a signal time window reduces the actual signal rate for the NTD configuration, while TES are practically unaffected, as reported in Fig. 6 (left). This could represent an issue when the size of natural crystals is too large or the source activity in doped crystals is too high. As shown in Fig. 6 (right), the different time resolutions considered do not introduce shape distortions to the energy spectrum, with the exception of the region near the decay Q -value, where this effect can be effectively modelled anyway.

To conclude, both TES and NTD are suitable for the ACCESS goals with the caveat that energy threshold and statistics losses due to poor time resolution may represent limiting factors for the second class of thermal sensors. In the case of InI, the optimal crystal size determines an activity way lower than 1 Hz, so the NTD sensor is still a good option; conversely for doped crystals we can increase the signal-to-background ratio optimising the doping level, which requires a TES if the signal rate exceeds the 1 Hz limit.

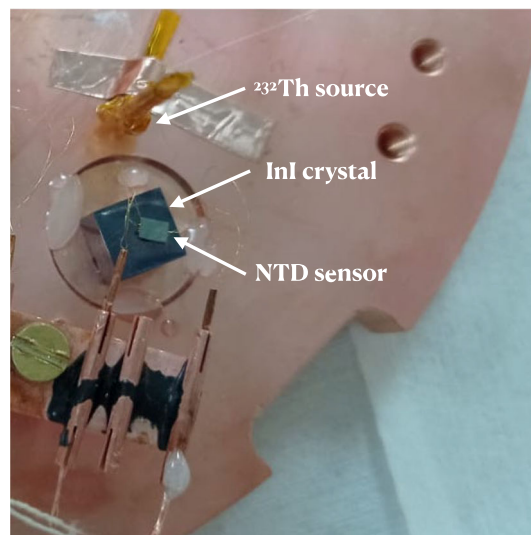


Fig. 7 Experimental setup used to measure the InI crystal as cryogenic calorimeter at LNGS. The detector is resting on the copper plate facing a ^{232}Th source

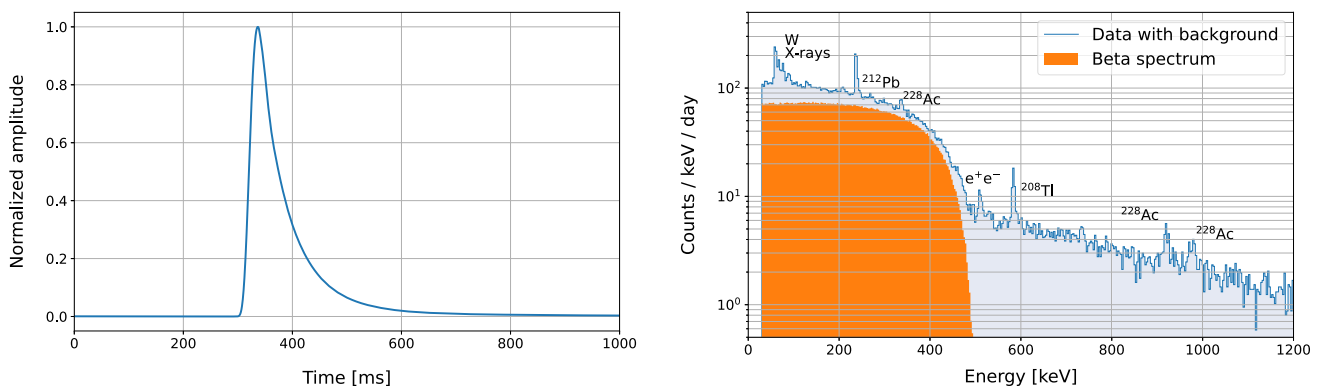


Fig. 8 *Left.* Template signal obtained by averaging hundreds of InI thermal pulses using a 1000 ms acquisition window. *Right.* Energy spectrum obtained with the InI crystal in 300 h of data taking together with the ^{115}In β -decay component (orange). The prominent γ -rays produced by a near ^{232}Th source are labelled

7 Preliminary measurements

Following the outcomes of the study presented in Sect. 6, we tested an indium iodide (InI) crystal of dimensions $7 \times 7 \times 7 \text{ mm}^3$ and mass 1.9 g. We equipped the InI crystal with an NTD thermistor ($3 \times 3 \times 1 \text{ mm}^3$), whose signal is readout with $25 \mu\text{m}$ gold wires. The detector was installed on a copper plate directly attached to the mixing chamber of the CUPID R & D cryostat and operated at 16 mK. We also added a ^{232}Th calibration source to the experimental setup, which is shown in Fig. 7.

The electronic readout and the data acquisition systems used in this measurement are described in Refs. [63, 64]. We saved on disk the continuum data stream, and every time the derivative trigger fired, a waveform of 1000 ms was recorded for InI. The collected data were then filtered with the optimum filter technique [65], following the standard steps established and tested by CUORE-0 [66], CUORE [48, 67], CUPID-0 [13, 68], and CUPID-Mo [14, 49] collaborations. In this configuration, we acquired over 300 h of physics data with a calibration source. The template pulse of the detector, obtained by averaging hundreds of signals, is presented in Fig. 8 (left). We calibrate InI using the prominent γ -ray peaks in the energy spectrum as presented in Fig. 7. Overall, the detector shows very good performance, achieving an energy threshold of 17 keV, and an energy resolution of 3.1 keV FWHM at 60 keV. Moreover, the dominant contribution in the spectrum is the β -decay of ^{115}In , as presented in Fig. 8 (right).

For the next steps of the project, we already established a collaboration to grow ^{99}Tc -doped crystals with a company which produced for ACCESS two $\text{TeO}_2 : ^{99}\text{Tc}$ crystals of dimensions $40 \times 35 \times 22 \text{ mm}^3$ and $35 \times 35 \times 22 \text{ mm}^3$, exploiting a ^{99}Tc -doped TeO_2 powder. At LNGS, we performed ICP-MS analysis of doped powder, filtered powder ready for the crystal growth and final crystals, measuring a ^{99}Tc concentration of (8 ± 2) ppb, (2.2 ± 0.2) ppb, and < 0.1 ppb, respectively. This preliminary material screening demonstrated that both powder filtering and crystal growth *purify* the crystal from ^{99}Tc . We also operated the two $\text{TeO}_2 : ^{99}\text{Tc}$ crystals as cryogenic calorimeters [69], obtaining from the data analysis an upper limit on concentration of ^{99}Tc of

0.01 ppb, well below the target value. Further tests and investigations are currently ongoing to understand the origin of the ^{99}Tc concentration reduction during the crystal production.

8 Conclusions

In this paper, we presented for the first time the ACCESS project, whose main goal is to develop cryogenic calorimeters to assess the spectral shape of forbidden β -decay. As first step, we proposed to measure the ^{115}In β -decay exploiting an InI natural crystal. The studies reported in Sec. 6 on InI demonstrate that a 7 mm side cubic crystal is an excellent compromise to optimise simultaneously the signal yield and the detector response function, avoiding efficiency loss induced by a high counting rate. Moreover, we proved that the time resolution of an NTD sensor (~ 10 ms) is suitable for this kind of crystal. On these bases, we tested an InI-based cryogenic calorimeter obtaining an excellent threshold of 17 keV, and an energy resolution of 3.1 keV FWHM at 60 keV. This achieved performance matches the ACCESS requirements and a further measurement of the InI detector with higher statistics is on the schedule.

Acknowledgements This project has received funding from the European Union's Horizon 2020 research and innovation program under the Marie Skłodowska-Curie Grant agreement N. 101029688. This work was supported by the Academy of Finland, Grant Nos. 314733, 320062 and 345869. We thank the CUPID collaboration for sharing their cryogenic infrastructure, M. Guetti for the assistance in the cryogenic operations, M. Perego for his invaluable help in many tasks, the mechanical workshop of LNGS. This work makes use of the DIANA data analysis and APOLLO data acquisition software which has been developed by the CUORICINO, CUORE, LUCIFER and CUPID-0 collaborations.



Funding Open access funding provided by Gran Sasso Science Institute - GSSI within the CRUI-CARE Agreement.

Data Availability Statement This manuscript has associated data in a data repository. [Authors' comment: The datasets generated and analysed during the current study are available in the B2SHARE repository, <https://doi.org/10.23728/b2share.ae08189026c44147bf747701fe97b1e0>.]

Open Access This article is licensed under a Creative Commons Attribution 4.0 International License, which permits use, sharing, adaptation, distribution and reproduction in any medium or format, as long as you give appropriate credit to the original author(s) and the source, provide a link to the Creative Commons licence, and indicate if changes were made. The images or other third party material in this article are included in the article's Creative Commons licence, unless indicated otherwise in a credit line to the material. If material is not included in the article's Creative Commons licence and your intended use is not permitted by statutory regulation or exceeds the permitted use, you will need to obtain permission directly from the copyright holder. To view a copy of this licence, visit <http://creativecommons.org/licenses/by/4.0/>.

References

1. J. Kotila, F. Iachello, Phys. Rev. C **85**, 034316 (2012). <https://doi.org/10.1103/PhysRevC.85.034316>
2. S. Stoica, M. Mirea, Phys. Rev. C **88**(3), 037303 (2013). <https://doi.org/10.1103/PhysRevC.88.037303>
3. J. Engel, J. Menéndez, Rep. Progr. Phys. **80**(4), 046301 (2017). <https://doi.org/10.1088/1361-6633/aa5bc5>
4. H. Ejiri, Front. Phys. (2019). <https://doi.org/10.3389/fphy.2019.00030>
5. J. Barea, J. Kotila, F. Iachello, Phys. Rev. C **91**(3), 034304 (2015). <https://doi.org/10.1103/PhysRevC.91.034304>
6. B. Märkisch et al., Phys. Rev. Lett. **122**, 242501 (2019). <https://doi.org/10.1103/PhysRevLett.122.242501>
7. J. Engel, J. Menéndez, Rept. Prog. Phys. **80**(4), 046301 (2017). <https://doi.org/10.1088/1361-6633/aa5bc5>
8. H. Ejiri, J. Suhonen, K. Zuber, Phys. Rep. **797**, 1 (2019). <https://doi.org/10.1016/j.physrep.2018.12.001>
9. A. Giuliani et al., Double Beta Decay APPEC Comm. Rep. (2019). <https://doi.org/10.48550/1910.04688>
10. J. Suhonen, Front. Phys. **5**, 55 (2017). <https://doi.org/10.3389/fphy.2017.00055>
11. M. Agostini et al., Nature **587**, 577 (2020). <https://doi.org/10.1038/s41586-020-2934-0>
12. P. Agnes et al., Phys. Rev. D **107**(6), 063001 (2023). <https://doi.org/10.1103/PhysRevD.107.063001>
13. O. Azzolini et al., Phys. Rev. Lett. **123**, 262501 (2019). <https://doi.org/10.1103/PhysRevLett.123.262501>
14. E. Armengaud et al., Eur. Phys. J. C **80**(7), 674 (2020). <https://doi.org/10.1140/epjc/s10052-020-8203-4>
15. D.Q. Adams et al., Phys. Rev. Lett. **126**, 171801 (2021). <https://doi.org/10.1103/PhysRevLett.126.171801>
16. M. Wang et al., Chin. Phys. C **41**(030003), 1674 (2017). <https://doi.org/10.1088/1674-1137/41/3/030002>
17. P. Belli et al., Phys. Rev. C **76**, 064603 (2007). <https://doi.org/10.1103/PhysRevC.76.064603>
18. L. Bodenstern-Dresler et al., Phys. Lett. B **800**, 135092 (2020). <https://doi.org/10.1016/j.physletb.2019.135092>
19. M. Laubenstein, B. Lehnert, S.S. Nagorny, S. Nisi, K. Zuber, Phys. Rev. C **99**, 045501 (2019). <https://doi.org/10.1103/PhysRevC.99.045501>
20. L. Pattavina et al., Eur. Phys. J. A **54**(5), 79 (2018). <https://doi.org/10.1140/epja/i2018-12515-5>
21. G.B. Beard, W.H. Kelly, Phys. Rev. **122**, 1576 (1961). <https://doi.org/10.1103/PhysRev.122.1576>

22. L. Pfeiffer, A.P. Mills, E.A. Chandross, T. Kovacs, Phys. Rev. C **19**, 1035 (1979). <https://doi.org/10.1103/PhysRevC.19.1035>
23. A.F. Leder et al., Phys. Rev. Lett. **129**(23), 232502 (2022). <https://doi.org/10.1103/PhysRevLett.129.232502>
24. O. Azzolini et al., Phys. Rev. D **100**(9), 092002 (2019). <https://doi.org/10.1103/PhysRevD.100.092002>
25. M. Loidl et al., Appl. Radiat. Isotopes **153**, 108830 (2019). <https://doi.org/10.1016/j.apradiso.2019.108830>
26. M. Gugiatti et al., Nucl. Instrum. Meth. A **979**, 164474 (2020). <https://doi.org/10.1016/j.nima.2020.164474>
27. A. Nava et al., Nucl. Instrum. Meth. A **1046**, 167812 (2023). <https://doi.org/10.1016/j.nima.2022.167812>
28. M. Haaranen, P.C. Srivastava, J. Suhonen, Phys. Rev. C **93**(3), 034308 (2016). <https://doi.org/10.1103/PhysRevC.93.034308>
29. M.T. Mustonen, M. Aunola, J. Suhonen, Phys. Rev. C **73**, 054301 (2006). <https://doi.org/10.1103/PhysRevC.76.019901>
30. E. Caurier et al., Rev. Mod. Phys. **77**, 427 (2005). <https://doi.org/10.1103/RevModPhys.77.427>
31. J. Toivanen, J. Suhonen, Phys. Rev. C **57**, 1237 (1998). <https://doi.org/10.1103/PhysRevC.57.1237>
32. M. Haaranen, J. Kotila, J. Suhonen, Phys. Rev. C **95**(2), 024327 (2017). <https://doi.org/10.1103/PhysRevC.95.024327>
33. F. Iachello, P.V. Isacker, The interacting boson-fermion model, in *Cambridge monographs on mathematical physics*. (Cambridge University Press, 1991)
34. A. Kumar, P.C. Srivastava, J. Kostensalo, J. Suhonen, Phys. Rev. C **101**, 064304 (2020). <https://doi.org/10.1103/PhysRevC.101.064304>
35. H. Behrens, W. Bühring, *Electron radial wave functions and nuclear beta-decay* (Clarendon Press, Oxford, 1982)
36. J. Kostensalo et al., Phys. Lett. B **822**, 136652 (2021). <https://doi.org/10.1016/j.physletb.2021.136652>
37. A. Kumar, P.C. Srivastava, J. Suhonen, Eur. Phys. J. A **57**, 225 (2021). <https://doi.org/10.1140/epja/s10050-021-00540-6>
38. E. Celi et al., Nucl. Instrum. Meth. A **1033**, 166682 (2022). <https://doi.org/10.1016/j.nima.2022.166682>
39. CMS-Collaboration, JINST **5**(03), T03010 (2010). <https://doi.org/10.1088/1748-0221/5/03/T03010>
40. L. Pattavina et al., JCAP **10**, 064 (2021). <https://doi.org/10.1088/1475-7516/2021/10/064>
41. J.W. Beeman et al., Eur. Phys. J. C **82**(8), 692 (2022). <https://doi.org/10.1140/epjc/s10052-022-10656-8>
42. N. Casali et al., J. Low Temp. Phys. **184**(3–4), 952 (2016). <https://doi.org/10.1007/s10909-016-1507-y>
43. E.E. Haller et al., *NTD germanium: a novel material for low temperature bolometers* (Springer, US, Boston, MA, 1984), pp.21–36
44. N.F. Mott, J.H. Davies, Philos. Mag. B **42**(6), 845 (1980). <https://doi.org/10.1080/01418638008222332>
45. N.F. Mott, Phil. Mag. J. Theor. Exp. Appl. **19**(160), 835 (1969). <https://doi.org/10.1080/14786436908216338>
46. A.L. Efros, B.I. Shklovskii, J. Phys. C Solid State **8**(4), L49 (1975). <https://doi.org/10.1088/0022-3719/8/4/003>
47. A. Giachero, J. Phys. Conf. Ser. **841**(1), 012027 (2017). <https://doi.org/10.1088/1742-6596/841/1/012027>
48. D.Q. Adams et al., Nature **604**(7904), 53 (2022). <https://doi.org/10.1038/s41586-022-04497-4>
49. C. Augier et al., Eur. Phys. J. C **82**(11), 1033 (2022). <https://doi.org/10.1140/epjc/s10052-022-10942-5>
50. K. Irwin, G. Hilton, *Transition-edge sensors* (Springer, Berlin Heidelberg, 2005), pp.63–150
51. J.N. Ullom, D.A. Bennett, Supercond. Sci. Tech. **28**(8), 084003 (2015). <https://doi.org/10.1088/0953-2048/28/8/084003>
52. K.E. Koehler, Appl. Sci. **11**(9), 4044 (2021). <https://doi.org/10.3390/app11094044>
53. V. Singh, et al., Submitted (2022). <https://doi.org/10.48550/arXiv.2210.15619>
54. G. Angloher et al., Astropart. Phys. **84**, 70 (2016). <https://doi.org/10.1016/j.astropartphys.2016.08.005>
55. R. Strauss et al., Nucl. Instrum. Meth. A **845**, 414 (2017). <https://doi.org/10.1016/j.nima.2016.06.060>
56. G. Angloher et al., Nucl. Instrum. Meth. A **1045**, 167532 (2023). <https://doi.org/10.1016/j.nima.2022.167532>
57. A. Armato et al., Phys. Rev. C **104**(1), 015501 (2021). <https://doi.org/10.1103/PhysRevC.104.015501>
58. R. Huang et al., JINST **16**(03), P03032 (2021). <https://doi.org/10.1088/1748-0221/16/03/P03032>
59. S. Nagorny et al., Nucl. Instrum. Meth. A **977**, 164160 (2020). <https://doi.org/10.1016/j.nima.2020.164160>
60. S. Agostinelli et al., Nucl. Instr. Meth. A **506**, 250 (2003). [https://doi.org/10.1016/S0168-9002\(03\)01368-8](https://doi.org/10.1016/S0168-9002(03)01368-8)
61. O. Azzolini et al., Eur. Phys. J. C **79**(7), 583 (2019). <https://doi.org/10.1140/epjc/s10052-019-7078-8>
62. A. Nucciotti et al., J. Phys. Conf. Ser. **1056**(1), 012039 (2018). <https://doi.org/10.1088/1742-6596/1056/1/012039>
63. C. Armaboldi et al., JINST **13**(02), P02026 (2018). <https://doi.org/10.1088/1748-0221/13/02/P02026>
64. S. Di Domizio et al., JINST **13**(12), P12003 (2018). <https://doi.org/10.1088/1748-0221/13/12/P12003>
65. E. Gatti, P.F. Manfredi, Riv. Nuovo Cim. **9N1**, 1 (1986). <https://doi.org/10.1007/BF02822156>
66. C. Alduino et al., Eur. Phys. J. C **77**(1), 13 (2017). <https://doi.org/10.1140/epjc/s10052-016-4498-6>
67. D.Q. Adams et al., Phys. Rev. Lett. **126**(17), 171801 (2021). <https://doi.org/10.1103/PhysRevLett.126.171801>
68. O. Azzolini et al., Phys. Rev. Lett. **129**(11), 111801 (2022). <https://doi.org/10.1103/PhysRevLett.129.111801>
69. D.L. Helis, et al., AIP Conference Proceedings **In Press** (2022)